2005 WSEAS Int. Conf. on REMOTE SENSING, Venice, Italy, November 2-4, 2005 (pp77-82)

A Contactless, Laser-Triangulation Based 3-D Measuring System For High-Speed Inspection of Glass Vessels

STEPHAN RUPP, CHRISTIAN MÜNZENMAYER, CHRISTIAN WINTER, KLAUS SPINNLER
Image Processing And Medical Engineering Department
Fraunhofer-Institute for Integrated Circuits IIS
Am Wolfsmantel 33, 91058 Erlangen
GERMANY

http://www.iis.fraunhofer.de

Abstract: - In the scope of quality inspection for glass vessels, we introduce a novel method to automatically evaluate 3-D range data acquired by a sheet-of-light sensor for the purpose of detecting discrepancies in the bottom measures of transparent vessels. We apply a histogram-based segmentation of the bottom's point clouds to automatically derive parameters for the classification of the inspected object. The major benefit is the high inspection speed meeting the requirements of 100% inspection in production lines running at a speed of three to ten bottles per second.

Key-Words: - Remote Sensing, Laser Triangulation, Range Imaging, Optical Inspection, Glass Bottles

1 Problem Statement

The fabrication of glass vessels for food, chemistry or pharmaceutical appliances requires a high production quality and process reliability. The product's compliance with the customer's specifications is of great importance for the customer and thus the manufacturer. For this reason, visual online inspection systems have become popular within quality assurance enabling the manufacturer to perform a 100% testing of their products. Due to the speed requirements of three to ten objects per second, contactless high speed solutions are necessary.

To our knowledge there exists no method in this field performing a survey of vessel's bottom based on 3-D data acquired by sheet-of-light imaging. Indeed, there are solutions emanating from related domains, but either they apply sheet-of-light technique to opaque object or they perform a pointwise measurement on transparent objects [1]. Tomography methods for an inspection of transparent pipes [2][3], flat glass inspection utilizing UV light [4] or coded-light appliances [5] suffer from processing speed or they are limitated to planar objects and do not compete with the former approaches as well as techniques gathering only 2-D information using transmitted-light methods in order to detect inclusions [6].

We introduce a technique, that is able to inspect vessels manufactured from glass in a fast and contactless manner. To be more specific, the method focusses on the surveying of the vessel's bottoms characterized by the three surfaces depicted in figure 1(c). The performance requirement of five bottles per second is met by the use of a dedicated 3-D range sensor scanning the bottoms as the objects are passing with a resolution of 1 mm in transport direction and 0.10 mm perpendicular to it.

The rest of the paper has the following structure. At first we present a short description of the measuring principle which is followed by remarks on the image acquisition and the sensor's calibration. Section 3 details the algorithm with results of different experiments being presented in section 4. The paper closes with a discussion and the conclusions.

2 Methods

2.1 Principle Of Measurement

The measuring principle for the acquisition of 3-D shapes is based on a method known as laser triangulation, or sheet-of-light range imaging. A classical configuration is depicted in figure 1(a), exhibiting the characteristics of such a system.

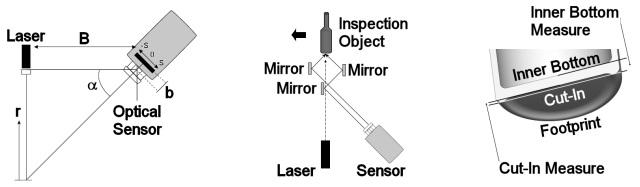

(a) (b) (c)

Figure 1: Classical laser-triangulation geometry (a) and the extended setup with 3 mirrors for the aquisition of two views from opposite directions (b). The surfaces of the inspected objects as well as the measures derived are depicted in (c).

A laser projects a thin line across the object with a camera looking at it from a different position under a certain angle which makes the straight laser line appear like the contour of a slice of the object. The range information derived from a contour line is often referred to as *profile* in laser triangulation systems. The 3-D shape of the object is finally built up profile by profile as it is passing the camera and the laser.

The information of interest is the profile or range vector $\mathbf{r}(t) \in \mathbb{R}^n$ rather than the complete image $\mathbf{I}(t) \in \mathbb{N}^{(m,n)}$. Therefore the laser's impact positions need to be estimated from the image leading to a sensor offset vector $\mathbf{s}(t) \in \mathbb{N}^n$. Once the offsets $s_i(t)$ have been extracted, the corresponding range values $r_i(t)$ can be calculated from the mapping $\mathcal{R} : \mathbb{N}^n \to \mathbb{R}^n$ defined by the triangulation geometry depicted in figure 1(b):

$$\mathcal{R} : \mathbb{N}^n \to \mathbb{R}^n : \mathbf{s}(t) \mapsto \mathbf{r}(t)$$
$$r_i(t) = B \tan\alpha - B \cdot \frac{b \tan\alpha - s_i(t)}{b + s_i(t) \tan\alpha} \qquad (1)$$

with

$$\mathbf{s}(t) = (s_0(t), \ldots, s_{n-1}(t)) \in \mathbb{N}^n$$
$$\mathbf{r}(t) = (r_0(t), \ldots, r_{n-1}(t)) \in \mathbb{R}^n$$

and where B denotes the baseline, b the distance between the camera's optical centre and the sensor plane, and α the viewing angle with respect to the baseline.

The profile acquisition depends on the diffus reflected parts of the incident light being responsible for the contour lines in the captured image. When the laser light strikes the object's surface only small parts of the radiance is diffuse reflected, with the remaining fraction entering the object along with certain refraction effects. When leaving a second diffuse reflection occurs, resulting in at least two laser line contours in the captured image (fig. 2).

Figure 2: The camera image $\mathbf{I}$ contains two laser line contours, one for the outer and one for the inner bottom surface. The mirror setup realizes a concept of redundancy enabling the recovery of lost data from two opposite viewing directions.

When inspecting non-coplanar surfaces occlusion effects occur, resulting in a loss of range data. This loss may also be caused by unintended total reflections. The encounter of such effects is based on an acquisition of redundant information. This is realized with one sensor observing a cubical inspection volume with 50 mm edge length via a system of three mirrors (fig. 1(b)) acquiring images from opposite directions (fig. 2).

2.2 Image Acquisition and calibration

In order to meet the requirements concerning processing speed, a dedicated range sensor is used, featuring a proprietary, intelligent CMOS image sensor with a resolution of 1536×512 pixel. The sensor is running an specialized firmware which enables the extraction of upto four offset vectors $\mathbf{s}^{(0)}(t), \ldots, \mathbf{s}^{(3)}(t)$ from the laser line contours. From a theoretical point of view, two lines are sufficient in order to derive planarity and parallism measures, but in practice the two additional lines can be utilized for error detection and correction purposes. The sensor and laser are both triggered by an external rotary encoder attached to the conveyor belt making the algorithms independent from its speed. In general, the mapping from the offset values $s_i(t)$ to range values $r_i(t)$ can be done by appliance of relation (1) yielding metric measures.

Due to construction-related reasons concerning the mirror configuration the sensor offsets are not aligned to the image axes resulting in sheared contour images (fig. 2). The correction of this distortion as well as the translation to metric heights is done by a mapping generated in a calibration step:

$$\mathcal{R}_{\text{cal}} : \mathbb{N}^n \to \mathbb{R}^n : \mathbf{s}(t) \mapsto \mathbf{r}(t).$$

While calibrating, a coplanar calibration target is used to scan the inspection volume, assigning in each step the observed sensor offset to the height the target is positioned at. These correspondences add up

to the mapping $\mathcal{R}_{\text{cal}}$ with missing values being linear interpolated.

3 Algorithm Outline

In the following, a range image with m rows, n columns and p planes is denoted as $\mathbf{A} \in \mathbb{R}^{(m,n,p)}$. The i^{th} plane is referenced by $\mathbf{A}^{(i)}$ with $A^{(i)}(x,y)$ representing the value of the pixel at (x,y) in the plane i.

3.1 Profile Processing

As mentioned above, at the time t the sensor provides the four offset vectors $\mathbf{s}^{(0)}(t), \ldots, \mathbf{s}^{(3)}(t)$ with one acquisition. These vectors are considered as the rows of a new created image with $\mathbf{s}^{(i)}(t)$ being assigned to the i^{th} plane, $i = 0, \ldots, 3$. By stacking subsequently acquired vectors, we get the range image $\mathbf{R}$, assuming the mapping $\mathcal{R}_{\text{cal}}$ has already been generated:

$$\mathbf{R}^{(i)} = \begin{pmatrix} \mathbf{r}^{(i)}(t_0) \\ \vdots \\ \mathbf{r}^{(i)}(t_{k-1}) \end{pmatrix} = \begin{pmatrix} \mathcal{R}_{\text{cal}}(\mathbf{s}^{(i)}(t_0)) \\ \vdots \\ \mathcal{R}_{\text{cal}}(\mathbf{s}^{(i)}(t_{k-1})) \end{pmatrix}.$$

The i^{th} plane $\mathbf{R}^{(i)}$ aggregates the profiles $\mathbf{r}^{(i)}(t_j)$ retrieved from k acquisitions at the times t_j. Due to the triggering, $\mathbf{R}$ consists of $k = 50$ rows carrying the undistorted metric height values.

3.2 Noise Removal

Unfortunately, the irregular surfaces produce unintended total reflections distorting the acquired range data. This effect is usually observable when the vessel enters or leaves the sheet-of-light and sporadic in between. Fortunatly, this kind of distortion is characterized by spurious outliers whereas the surfaces' range values share generally similar levels. This justifies the calculation of an intermediate histogram $h_{\mathbf{R}}(r)$, exhibiting noticeable peaks for the surfaces of interest and low frequencies for the outliers (fig. 4(b)). Due to this observation all range values $R^{(i)}(x,y)$ exceeding the range threshold r_{th} are suppressed resulting in the enhanced image $\hat{\mathbf{R}}$:

$$\hat{R}^{(i)}(x,y) = \begin{cases} 0 & \begin{smallmatrix} h_{\mathbf{R}}(R^{(i)}(x,y)) < h_{\text{th}} \\ \wedge\ r_{\text{th}} < R^{(i)}(x,y) \end{smallmatrix} \\ R^{(i)}(x,y) & \text{otherwise} \end{cases} \quad (2)$$

The parameter r_{th} references the right most range value surpassing a certain frequency threshold $h_{\text{th}} = h_{\mathbf{R}}(r_{\text{th}})$ and corresponds typically to the footprint.

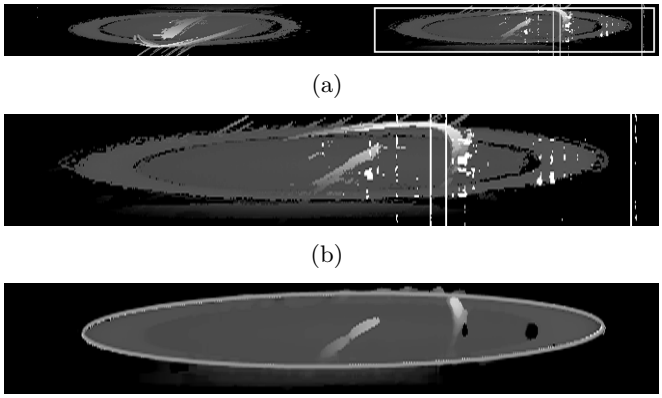

(a)

(b)

(c)

Figure 3: Greyscale representations of the incoming range image $\mathbf{R}$ (a), the zoomed right view showing typical distortions (b) and the same section noise-filtered overlaid with a fitted ellipse E_{r} that is utilized for the alignment of the both views (c).

With h_{th} the highest valid range value is automatically computed from the histogram realizing an effective and adaptive outlier removal.

3.3 Recovery of Lost Data

In order to recover pertubated data, both of the views are aligned with each other. For this reason, the noise-filtered range image $\hat{\mathbf{R}}$ is converted into a grayscale image followed by a median filtering. From the filtered image's first plane the bottle's boundary points are extracted, serving as control points for a non-iterative ellipse fitting [7]. We make use of an implementation [8] that was essentially improved with respect to numerical stability and computational effort.

The results are two ellipses E_{l} and E_{r} approximating the boundary of the vessel (fig. 3(c)). From these ellipses an affine transformation

$$\mathbf{A}(\mathbf{x}) = \begin{pmatrix} S_x & 0 \\ 0 & S_y \end{pmatrix} \left(\mathbf{x} - \begin{pmatrix} t_x \\ t_y \end{pmatrix} \right), \mathbf{x} = \begin{pmatrix} x \\ y \end{pmatrix}$$

is derived mapping the content of the right ellipse to the left. Applied to the range image $\hat{\mathbf{R}}$ the views are aligned by:

$$\mathcal{A} : \mathbb{R}^{(m,n,p)} \rightarrow \mathbb{R}^{(m,\frac{n}{2},2p)} : \hat{\mathbf{R}} \mapsto \tilde{\mathbf{R}}$$

$$\tilde{R}^{(i)}(\mathbf{x}) = \begin{cases} \hat{R}^{(i)}(\mathbf{x}) & 0 \leq i < p \wedge \mathbf{x} \in E_{\text{l}} \\ \hat{R}^{(i)}(\mathbf{A}(\mathbf{x})) & p \leq i < 2p \wedge \mathbf{x} \in E_{\text{r}} \end{cases}$$

So, the aligned range image $\tilde{\mathbf{R}}$ emerges from $\hat{\mathbf{R}}$ by storing the pixel $\hat{R}^{(i)}(x,y)$ covered by the left ellipse

in the planes $\tilde{\mathbf{R}}^{(i)}, i = 0, \ldots, (p-1)$ and those covered by the right ellipse at the transformed locations in the planes $\tilde{\mathbf{R}}^{(i)}, i = p, \ldots, (2p-1)$.

3.4 Orientation Correction

Caused by positioning tolerances, in most cases the vessel's bottom will not be in parallel to the x-y plane which prevents prominent histogram peaks. For this reason, its orientation has to be estimated, realized by fitting a plane into the range values forming its footprint. The control points are extracted from the aligned image $\tilde{\mathbf{R}}$ by applying the following steps for each of the $k = 50$ rows:

1. Assemble a new line $\mathbf{v}_k = (v_0, \ldots, v_n)$ from the aligned lines $\tilde{\mathbf{r}}_k^{(0)}$ and $\tilde{\mathbf{r}}_k^{(4)}$. If $\tilde{R}^{(0)}(x,k)$ is valid and $\tilde{R}^{(4)}(x,k)$ not, set $v_x = \tilde{R}^{(0)}(x,k)$ and vice versa, pick the average if both are valid: $v_x = \frac{1}{2}\left(\tilde{R}^{(0)}(x,k) + \tilde{R}^{(4)}(x,k)\right)$.

2. Apply a 1-D median filter to $\mathbf{v}_k$ removing spurious outliers.

3. Add the left most and right most maximum to the initially empty set $\tilde{C}$:

$$\tilde{C} \cup \{(\arg\max V_l, k, \max V_l)'\}$$
$$\tilde{C} \cup \{(\arg\max V_r, k, \max V_r)'\}$$

with

$$V_l = \{v_0, \ldots, v_n\}$$
$$V_r = \{v_n, \ldots, v_0\}$$

In order to attain a more robust fit, every element $\mathbf{p} = (p_x, p_y, p_z)' \in \tilde{C}$ is removed not satisfying

$$|p_z - \mu| < \sigma$$

where μ denotes the average and σ the standard deviation of the third component of all $\mathbf{p} \in \tilde{C}$. From the remaining set the plane $F : \mathbf{n} \cdot \mathbf{x} - d = 0$ is calculated by a least-squares method described in [9].

The roll and pitch angles of the footprint plane encode the vessel's pose and they are utilized to compute a mapping yielding an alignment with the x-y plane. For this reason, the new plane $F_{\text{ref}} : \mathbf{n}_{\text{ref}} \cdot \mathbf{x} - d = 0$, $\mathbf{n}_{\text{ref}} = (0,1,0)'$ is defined and referred to as *reference plane*. Considering the range image $\tilde{\mathbf{R}}$, we are solely interested in its values $\tilde{R}^{(i)}(x,y)$ and

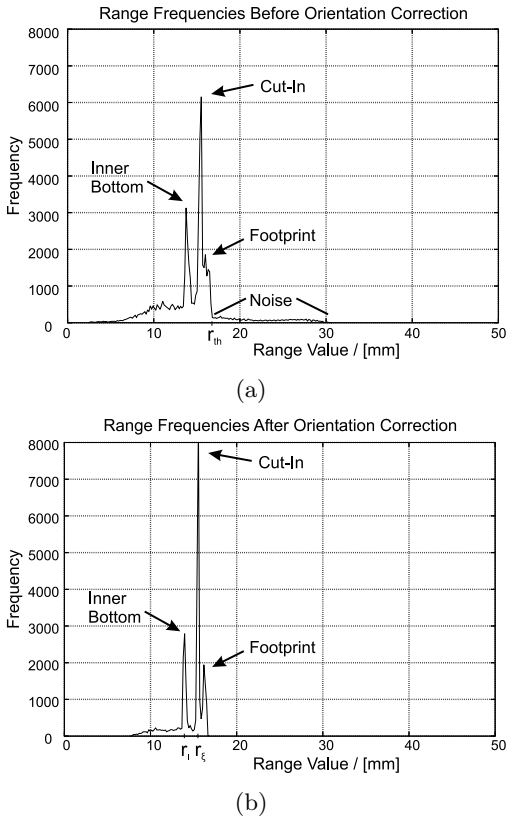

Figure 4: The peak for the footprint of a tilted bottle cannot clearly identified (a). After orientation correction the footprint and the the cut-in are separated from each other (b).

the relationship between them. Since their locations (x,y) are of no importance, it is sufficient to perform a shearing transformation rather than a more expensive rotation:

$$\breve{R}^{(i)}(x,y) = \tilde{R}^{(i)}(x,y) + \underbrace{(\mathbf{n} \cdot (x,y,d)' - d)}_{\Delta(F_{\text{ref}},F)} ,$$

where $\Delta(F_{\text{ref}}, F)$ describes the perpendicular distance between F_{ref} and F at (x,y). After orienation correction the range values are aligned to the x-y plane, resulting in distictive peaks for the surfaces (see fig. 4(b)).

3.5 Surface Assignment and Measures Definition

Based on the corrected range image $\breve{\mathbf{R}}$, a final histogram $h_{\breve{\mathbf{R}}}(r)$ is calculated and utilized to assigned the range values to the surfaces they correspond to. Regarding the cut-in surface, the right most peak position r_ζ is extracted from the histogram. Starting at this point, the histogram is searched to the left for the position $r_{\zeta 1}$ where the frequency falls below a certain

threshold $h_{\breve{\mathbf{R}}}(r_{\zeta \mathrm{l}}) < h_\zeta$ – analogously is performed for the right search direction. The set of 3-D points forming the cut-in is then given by

$$P_\zeta = \{(x, y, \breve{R}^{(i)}(x, y))' : r_{\zeta \mathrm{l}} \leq \breve{R}^{(i)}(x, y) \leq r_{\zeta \mathrm{r}}\}$$

In the same way is processed for the inner bottom yielding the position $r_{\iota \mathrm{l}}$ and $r_{\iota \mathrm{r}}$ according to the threshold h_ι. Again, the set of 3-D points is given by

$$P_\iota = \{(x, y, \breve{R}^{(i)}(x, y))' : r_{\iota \mathrm{l}} \leq \breve{R}^{(i)}(x, y) \leq r_{\iota \mathrm{r}}\}$$

Finally, referring to the reference plane F_{ref}, distances between F_{ref} and the elements $\mathbf{p}$ of the point clouds P_ζ and P_ι are calculated giving rise to parallism and planarity measures.

We distinguish between *inner* and *outer* measures. The latter are not subject to any refraction effects and are defined as follows:

$$\begin{aligned} \zeta_{\min} &= \min_{\mathbf{p} \in P_\zeta} (\mathbf{n}_{\mathrm{ref}} \cdot \mathbf{p} - d) \\ \zeta_{\max} &= \max_{\mathbf{p} \in P_\zeta} (\mathbf{n}_{\mathrm{ref}} \cdot \mathbf{p} - d) \\ \zeta_{\mathrm{obliquity}} &= \zeta_{\max} - \zeta_{\min} \end{aligned}$$

where the arguments of the minimum and maximum operators represents the perpendicular distance of the point $\mathbf{p}$ to the reference plane $F_{\mathrm{ref}} : \mathbf{n}_{\mathrm{ref}} \cdot \mathbf{p} - d = 0$.

In contrast to the cut-in, refraction effects have to be taken into account for the inner measures. Since refraction affects only the portion of light penetrating the glass, only the distance $d_{\mathrm{g}}(\mathbf{p})$ denoting the perpendicular distance of $\mathbf{p}$ to the cut-in has to be corrected, while the portion penetrating the air is unaffected:

$$\begin{aligned} \iota_{\min} &= \min_{\mathbf{p} \in P_\iota} [(\mathbf{n}_{\mathrm{ref}} \cdot \mathbf{p} - d) - \delta(\mathbf{p})] \\ \iota_{\max} &= \max_{\mathbf{p} \in P_\iota} [(\mathbf{n}_{\mathrm{ref}} \cdot \mathbf{p} - d) - \delta(\mathbf{p})] \\ \iota_{\mathrm{obliquity}} &= \iota_{\max} - \iota_{\min} \end{aligned}$$

with

$$\delta(\mathbf{p}) = d_{\mathrm{g}}(\mathbf{p}) \cdot (1 - \rho)$$

and ρ modelling the refraction effect. $d_{\mathrm{g}}(\mathbf{p})$ is subject to a plane, that has been fitted into the set of cut-in points P_ζ. In fact, the influence of the effect depends on the material's refraction index, the surface's orientation and therefore an orientation-aware correction factor would be more suitable, than a simplifying constant factor.

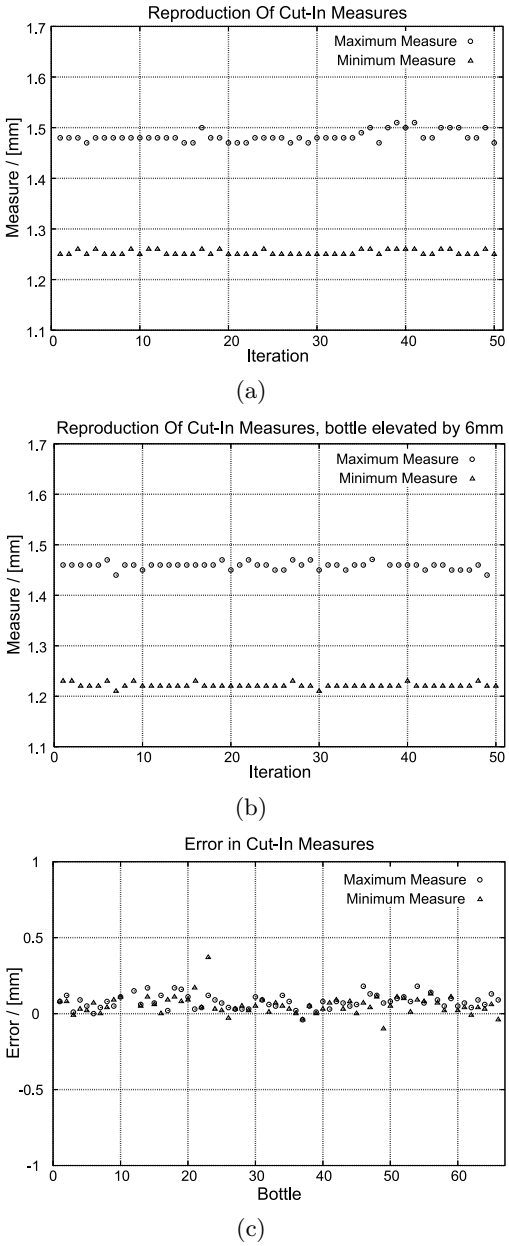

Figure 5: Experiments exhibit small deviations in the cut-in's measures when testing single bottles repeatedly (a)(b) and an over-all error smaller than 0.20 *mm* with respect to a reference sample of 64 vessels (c).

4 Results

We have evaluated the system in our laboratory as well as in a production line with a reference random sample of 66 vessels. In the following, we exemplarily present the results for the cut-in measures.

The first experiment was designed to prove evidence that the system derives almost the same measures for identical vessels. For this reason a bottle is presented to the inspection system repeatedly. The

results are depicted in figure 5(a) showing the performance of the inspections for a bottle with a reference cut-in minimum measure of 1.24 mm and 1.44 mm maximum measure. The repeated inspections results in 1.25 mm on average with a standard deviation of 0.004 mm for the minimum measures and an average of 1.48 mm with with a standard deviation of 0.010 mm for the maximum measures respectively.

The measurement's sensivity with respect to different locations of the vessels within the inspection volume is in the focus of the second test (fig. 5(b)). Again a bottle is inspected repeatedly but lifted by 6 mm and rotated by 90 degree around its normal axis, simulating different altitudes in real production environment. Now, the cut-in's average is 1.22 mm for the minimum and 1.43 mm for the maximum. The standard deviation for the minimum amounts 0.004 mm whereas 0.011 mm for the maximum measures. Relating the results to the system's theoretical resolution of 0.08 mm reveals the good performance of the algorithm.

In a third experiment, we concentrate on the errors in the measurements concerning the outer and inner surface when inspecting a sequence of known vessels. The error in the cut-in measures is depicted in figure 5(c) showing a discrepancy of 0.03 mm with respect to the minimum measures and 0.07 mm for the maximum measures – the standard deviation is 0.05 mm.

Due to the simplification of refraction, the inner measures perform in general slightly worse. As a lower bound for the accuracy concerning inner measure 0.20 mm has been identified from the experiments, whereas an upper bound for the accuracy of outer measures is given by 0.10 mm.

Test running with a conveyer belt in a manufacturing line reveal comparable results to those proven by the experiments on the laboratory.

5 Discussion And Conclusions

We presented a technique, that is able to inspect vessels manufactured from glass in a fast and contactless manner. We described a histogram-based algorithm enabling the removal of unintended reflections as well as an assignment of the range data to the inner and outer surfaces. Metric measurements are derived in a reproducible manner with an accuracy of 0.10 mm concerning the outer measures and 0.20 mm for those related to the inner surface.

The method requires almost aligned surfaces in order to make the histogram-based approach work. Indeed, bottles exhibiting strong oblique bottoms are classified in the right way, but they lack of correct metric measures. This is due to the algorithm's design that is based on the identification of concentrations of equal or similar range values resulting in distincitve peaks. When regarding vessels possessing strong oblique bottoms, these peaks will disappear making an extraction of the surfaces harder or impossible.

Promising improvements are likely realizable in a more sophisticated modelling of refraction effects and a prior registration of the left and right view, remedying the inaccuracies when extracting control points for the ellipse fitting.

References

[1] Leikas E., Haajanen L., and Kuusela H. Windscreen Shape Measurements in 3-D with a Video Camera System. In *Proc. of Automation 95*. Helsinki, 1995.

[2] Lang P. 3-D-Inspection of Transparent Pipes. In *Proc. 3-D Image Analysis and Synthesis, Erlangen*, November 1996.

[3] Schmidt R., Schramm U., Hofmann R., Caulier Y., Spinnler K., and Wittenberg T. Automatic three-dimensional Inspection, Measurement and Detection of Errors in Transparent Pipes. In *Proc. of 5th Int. Fall Workshop Vision, Modeling, and Visualization 2000*, November 2000.

[4] Leikas E. and Yli-Vakkuri E. Improved Glass Measuring System. In *Proc. Glass Processing Days*. September 13-15, 1997, Tampere, Finland, Septmeber 1997.

[5] Koch A., Ruprecht M., and O.Toedter G.H. *Optische Messtechnik an technischen Oberflächen*. Expert Verlag, Renningen-Malmsheim, 1998.

[6] Li X., Fang Z., Chow S., and Lim J. In-Situ Inspection of Inclusions in Thoughened Glass Panels. *The 3rd International Conference on Experimental Mechanics*, 2004.

[7] Fitzgibbon A., Pilu M., and Fisher R. Direct Least Square Fitting Of Ellipses. *Intern. Conference on Pattern Recognition*, 1996, pp. 253–257.

[8] Flusser J. and Halir R. Numerically Stable Direct Least Square Fitting Of Ellipses. *International Conference on Computer Graphics, Visualization and Interactive Digital*, vol. 1, 1998, pp. 125–132.

[9] Feddema J.T. and Little C.Q. Rapid World Modelling: Fitting Range Data to Geometric Primitives. *Intern. Conference on Robotics And Automation*, 1997, pp. 2807–2812.